Chemical Science

Accepted Manuscript

Chemical Science

rsc.li/chemical-science

Volume 9
Number 1
7 January 2018
Pages 1-268

ISSN 2041-6539

ROYAL SOCIETY OF CHEMISTRY

EDGE ARTICLE
Xinjing Tang et al.
Caged circular siRNAs for photomodulation of gene expression in cells and mice

ROYAL SOCIETY OF CHEMISTRY

rsc.li/chemical-science

ARTICLE

Manipulating Spin-state Conversion to Promote Asymmetric d-p Orbital Hybridization for High-Efficiency Nitrate Electroreduction to Ammonia

Ke Wang,‡[a] Tong Zhao,‡[a] Hou Wang,[b] Shiyu Zhang,[a] Rupeng Wang,[a] Meng Wang[a], Zixiang He,[a] Nan-Qi Ren[a], and Shih-Hsin Ho*[a]

Electrochemical nitrate reduction reaction (eNO$_3^-$RR) presents a sustainable solution for water pollutant management and green ammonia (NH$_3$) synthesis. However, hindered by spin-forbidden barrier, the sluggish hydrogenation kinetics of the key intermediate *NO severely limits the production of NH$_3$. Here, we reported for the first time the realization of a controllable transition of the inner Co spin-state from a low spin to a high spin in CuCo$_2$O$_4$ through the Mn doping-driven oxygen vacancies strategy (Mn-CuCo$_2$O$_{4-x}$). The elevated Co spin-state enhanced Co 3d (d$_{xz}$/d$_{yz}$/d$_z^2$)-*NO 2p asymmetrical orbital hybridization, facilitating *NO intermediates adsorption and the subsequent hydrogenation. Thanks to the Cu-Co synergistic effect enhanced via spin-state modulation, the Mn-CuCo$_2$O$_{4-x}$/graphene oxide aerogel (GAs) exhibited an attractive NH$_3$ yield rate of 2.14 mg/h/cm^2 with a dramatic NH$_3$ Faradic efficiency of 98.37% at environmentally relevant NO$_3^-$ level (10 mM NO$_3^-$-N), far superior to the Co$_3$O$_4$/GAs, CuCo$_2$O$_4$/GAs and as-reported catalysts. Moreover, the strong interfacial interaction between GAs and Mn-CuCo$_2$O$_{4-x}$ suppresses structural reconstruction of Mn-CuCo$_2$O$_{4-x}$, endowing the hybrid with robust stability. Herein, we confirm spin-state modulation can enhance the Cu-Co synergistic effect and reveal a universal strategy to optimize intermediate adsorption/conversion through spin-state, opening up a new avenue for deep purification of water pollutants based on spin optimization and providing general principles for the rational design of catalytic materials.

1. Introduction

Increasingly serious problems of nitrogen cycle disruption and environmental contamination pose significant threats to global ecosystem and public health.[1-3] Nitrate (NO$_3^-$), a predominant contaminant in industrial effluents and agricultural runoff, is identified as a critical contributor to eutrophication, drinking water pollution and ecosystem disruption.[4, 5] Concurrently, ammonia (NH$_3$) serves as the core raw material for agricultural fertilizers and clean hydrogen energy carriers. The conventional NH$_3$ production method depends on the energy-consuming Haber-Bosch process, generating a considerable carbon footprint.[6, 7] The electrochemical nitrate reduction reaction (eNO$_3^-$RR) can convert NO$_3^-$ into value-added NH$_3$ under mild conditions, providing a sustainable solution to the above dual challenges.[8-10] Despite its promise, the practical implementation of eNO$_3^-$RR is fundamentally throttled by the kinetically sluggish hydrogenation of a critical intermediate (*NO), where a spin-forbidden barrier imposes severe limitations on reaction rates and Faradaic efficiency (FE).

The hydrogenation of *NO constitutes the rate-determining step (RDS) in eNO$_3^-$RR, as its spin-polarized triplet ground state inherently resists to form singlet *HNO intermediates—a classic manifestation of spin selection rules. Although the Cu-Co bimetallic system in eNO$_3^-$RR partially mitigate this kinetic barrier through functional decoupling, in which Cu site preferentially adsorbs NO$_3^-$ and drives the initial deoxygenation reaction, and the Co site is responsible for the subsequent *NO hydrogenation conversion.[11-13] However, current design paradigms predominantly focus on macro/meso-structure engineering (e.g., alloying, defect modulation, reconstruction).[14-16] These approaches fail to deeply modulate the essential electronic structure determinants. As a core feature of the d-orbital electron arrangement of transition metals, spin-state can significantly change the orbital adsorption strength and hybridization mode of metal-intermediates, thereby impacting the reaction process.[17] Spinel-type CuCo$_2$O$_4$ is an ideal platform for resolving Co spin-state effect due to its unique structural tunability. Co^{3+} occupies octahedral site in CuCo$_2$O$_4$, and its spin-state is significantly affected by the local coordination environment and lattice stresses.[18] Some studies have shown that by introducing hetero-atoms for doping in Co-based materials to induce lattice distortions, the ligand field strength of Co^{3+} can be effectively tuned, consequently enabling controllable switching of spin-state.[19-21]

a. State Key Laboratory of Urban Water Resource and Environment, School of Environment, Harbin Institute of Technology, Harbin, 150040, P. R. China.
b. College of Environmental Science and Engineering and Key Laboratory of Environmental Biology and Pollution Control (Ministry of Education), Hunan University, Changsha, 410082 China

‡ These authors contributed equally to this work.

Chemical Science Accepted Manuscript

The spin-state of the Co sites critically determine the d-orbital energy level configuration, where the HS state exhibits stronger ligand field splitting effects and higher occupancy in the e_g orbitals.[22, 23] This electronic configuration enhances the adsorption and activation of reaction intermediates through optimized orbital interactions, thereby facilitating the RDS in catalytic processes.[24] Notably, compelling theoretical and experimental validation for such spin-dependent electronic modulation effects exists in analogous spin-sensitive electrochemical processes, such as the oxygen reduction and evolution reactions, yet this potent strategy remains conspicuously unexplored and underutilized within the eNO$_3^-$RR framework.[25, 26] Consequently, it is imperative to elucidate whether HS Co sites can indeed enhance *NO adsorption and accelerate its hydrogenation kinetics through changing the orbital hybridization pattern with the *NO intermediate and to unravel the interplay between the Co spin-state and the established Cu-Co synergistic effect. These interesting validations will unlock unprecedented activity and selectivity for the next generation of NO$_3^-$ reduction electrocatalysts.

Here, we utilized CuCo$_2$O$_4$ as a model catalytic system and proposed a Mn doping-driven oxygen vacancies strategy to precisely modulate the spin-state of Co. Experimental studies demonstrate that HS state Co can greatly optimize the adsorption of *NO and solve the problem of slow hydrogenation kinetics in the RDS (*NO→*HNO) via enhancing the asymmetric hybridization of the Co 3d ($d_{xz}/d_{yz}/d_{z^2}$)-*NO 2p orbitals. This spin state-optimized bimetallic synergistic effect endowed Mn-CuCo$_2$O$_{4-x}$/GAs with excellent catalytic performance (Faradaic efficiency (FE): 98.37%, yield rate: 2.14 mg/h/cm^2 at -0.6 V vs. RHE, 10 mM NO$_3^-$-N), exceeding Co$_3$O$_4$/GAs, CuCo$_2$O$_4$/GAs and as-reported catalysts. This work provides a theoretical paradigm for extending the spin-engineering strategy to bimetallic synergistic catalytic system, while also inaugurates a new dimension of electronic structure modulation for designing efficient NO$_3^-$ conversion catalysts.

2. Experimental section

2.1 Chemicals
All chemical reagents were depicted in Text S1.

2.2 Catalyst Preparation

2.2.1 Preparation of GAs. Graphene aerogels (GAs) were synthesized by hydrothermal combined calcination method. A standard synthesis protocol involved homogenizing 60 mg carboxymethyl cellulose (CMC) with 30 mL graphene oxide (GO) (2 mg mL^{-1}) under ultrasonic processing for 60 min. This precursor solution underwent hydrothermal treatment at 180 °C for 12 h. The synthesized hydrogels were purified using deionized water, freeze-dried, and then thermal treatment at 900 °C for 2 h under N$_2$ flow to generate GAs. Finally, the GAs was functionalized with 0.2 ml aminopropyltriethoxysilane (APTES) to impart positive surface charge.

2.2.2 Preparation of Mn-CuCo$_2$O$_{4-x}$ yolk-shell spheres. A blend of Cu(NO$_3$)$_2$·3H$_2$O (0.1 mmol), Co(NO$_3$)$_2$·6H$_2$O (0.2 mmol), a certain amount of Mn(NO$_3$)$_2$·6H$_2$O, and 8 mL glycerol was introduced into 40 mL isopropanol, stirred to obtain

homogenous solution. This solution was moved into a 100 mL solvothermal reaction vessel lined with Teflon and maintained at a temperature of 180 °C over 6 h. The resulting precursor from the solvothermal reaction was given a dual centrifugal rinse using deionized water and ethanol before undergoing a 12 h drying phase at 80 °C. The Mn-CuCo$_2$O$_{4-x}$ yolk-shell spheres were then generated by placing the dried precursor in a tube furnace set at 400 °C and sustained for 1 h under O$_2$ condition. Co$_3$O$_4$ and CuCo$_2$O$_4$ were prepared similarly to the Mn-CuCo$_2$O$_{4-x}$ except that the corresponding metal salts were not added.

2.2.3 Preparation of Mn-CuCo$_2$O$_{4-x}$/GAs. The Mn-CuCo$_2$O$_{4-x}$/GAs composite was self-assembled from GAs and CuCo$_2$O$_4$. More specifically, an initial step involves dispersing 0.1 g Mn-CuCo$_2$O$_{4-x}$ yolk-shell spheres in an isopropanol solution loaded with poly(sodium 4-styrenesulfonate) (PSS) (concentration: 0.2 mL PSS, 20 mL isopropanol), yielding PSS-treated Mn-CuCo$_2$O$_{4-x}$ yolk-shell spheres. These spheres were subsequently cleaned twice by centrifugation using alcohol and deionized water. The cleaned product was then dispersed in deionized water and gently added to a GAs suspension (60 ml, 0.5 mg mL^{-1}), stirring for 180 min to achieve a dispersion of Mn-CuCo$_2$O$_{4-x}$/GAs composite material. Mn-CuCo$_2$O$_{4-x}$/GAs composite material was isolated via vacuum filtration, sequentially purified with ethanol-aqueous solution under ambient condition. Co$_3$O$_4$/GAs and CuCo$_2$O$_4$/GAs were prepared in the same procedure as Mn-CuCo$_2$O$_{4-x}$/GAs.

2.2.4 The preparation of working electrode.
10 mg of the catalysts were re-dispersed into 470 µL of ethanol and 470 µL of deionized water, followed by adding 60 µL of Nafion solution to make a homogeneous solution. Subsequently, it was ultrasonicated for about 1 h to enable the well dispersion of catalyst inks. Afterwards, 100 µL of catalyst inks were dropped onto the carbon paper with an area of 1 cm2 (1 cm × 1 cm).

2.3 Characterization
More details on the characterization methods were provided in the Supplementary Information (Text S2).

2.4 Electrochemical measurements
The electrochemical tests were performed using a three-electrode system connected to the CHI 760E electrochemical workstation in a typical H-cell. The H-cell was separated by a Nafion 117 membrane (Dupont) that was pretreated following reported procedures. The catalysts were used as the working electrode, while Ag/AgCl electrode and platinum mesh were used as the reference and counter electrodes, respectively. The electrolytes were Ar-saturated 0.1 M Na$_2$SO$_4$ containing 10 mM NO$_3^-$-N. All potentials were calibrated to the reversible hydrogen electrode (RHE) scale by the Nernst equation (E_{RHE} = $E_{Ag/AgCl}$ + 0.197 V + 0.059 V × pH). The current density was normalized to the geometric electrode area (~1 cm^2). The linear sweep voltammetry (LSV) test was carried out in a three-electrode system at scanning rates of 10 mV s^{-1}. Electrochemical impedance spectra (EIS) measurements were conducted in a frequency range from 10^5 to 0.01 Hz with 5 mV amplitude. Cyclic votammetry (CV) curves were conducted in non-Faradaic region with different scan rates (20, 40, 60, 80, and 100 mV s^{-1}).

2.5 Analytical methods

Details information of nitrogen species concentration determination and the calculation of the eNO_3^-RR parameters were provided in Text S3 and Text S4, respectively. Detailed steps of *In-situ* Fourier transformed infrared spectroscopy (FT-IR), online differential electrochemical mass spectrometry (DEMS), and electron spin resonance (ESR) measurements were described in Text S5, Text S6, and Text S7, respectively. Density functional theory (DFT) calculations were presented in Text S8.

3. Results and discussion

3.1 Catalyst Characterization

The preparation process of the Mn-$CuCo_2O_{4-x}$/GAs composite framework is shown in Figure 1a. First, Mn-$CuCo_2O_{4-x}$ yolk-shell nanospheres were prepared via solvothermal combined high-temperature calcination. Subsequently, Mn-$CuCo_2O_{4-x}$/GAs was synthesized via a charge neutralization process. A thorough examination of the microstructure of Mn-$CuCo_2O_{4-x}$ was conducted using scanning electron microscopy (SEM) and transmission electron microscopy (TEM). The Mn-$CuCo_2O_{4-x}$ possessed a well-defined yolk-shell architecture, as clearly observed in Figures 1b- c, characterized by an average particle diameter of approximately 400 nm and distinct surface roughness. Selected area electron diffraction (SAED) analysis confirmed the polycrystalline characteristics of the Mn-$CuCo_2O_{4-x}$ (Figure 1d). Elemental mapping via energy-dispersive spectroscopy (EDS) confirmed homogeneous spatial distribution of Mn, Cu, Co, and O constituents throughout the yolk-shell spheres (Figures 1e-i). Inductively coupled plasma mass spectrometry (ICP-MS) quantified Mn content at 9.36 wt% (Table S1). The combined results from EDS and ICP-MS analysis conclusively verified the successful incorporation of Mn within the composite structure. The Mn-CuCo glycerate precursors underwent structural evolution into yolk-shell architectures via the Ostwald maturation mechanism, as also supported via comparative TEM analyses of Co_3O_4 and $CuCo_2O_4$ phases (Figures S1-S4).[27] To impart the Mn-$CuCo_2O_{4-x}$ with negative electrical properties, we utilized PSS for its modification via electrostatic self-assembly. During the PSS modification process, the sulfonic acid group (SO_3^-) of PSS would be adsorbed on the surface of Mn-$CuCo_2O_{4-x}$ through electrostatic interaction, forming a stable negatively charged layer (Figure S5).[28] Simultaneously, the amino group (-NH_2) of APTES molecule underwent a protonation reaction with protons in solution to form positively charged ammonium ions (-NH_3^+), and -NH_3^+ was stably anchored to the surface of the GAs via covalent bonds, thus conferring a positively charged character.[29] Then, the oppositely charged Mn-$CuCo_2O_{4-x}$ and GAs were mixed to form the Mn-$CuCo_2O_{4-x}$/GAs composites in situ through a charge neutralization process. As illustrated in Figures 1j-k, Mn-$CuCo_2O_{4-x}$ was embedded into the 3D porous skeleton of GAs to form a stable Mn-$CuCo_2O_{4-x}$/GAs composite framework. The introduction of GAs promoted rapid electron transport while effectively maintaining the stability of the structure, as will be detailed in the subsequent stability characterization section. High-resolution TEM (HRTEM) image demonstrated clear lattice streaks and GA layers, and the measured crystal plane spacing

of 0.245 nm corresponded to the (311) crystal plane of $CuCo_2O_4$, confirming that the spinel structural features were maintained after Mn doping (Figure 1l). TEM images of Co_3O_4/GAs and $CuCo_2O_4$/GAs composites suggested that Co_3O_4 and $CuCo_2O_4$ were also tightly coupled to the GAs scaffolds, thus confirming the general applicability of the charge neutralization strategy in constructing metal oxide/GAs composites (Figures S6-S7).

The successful synthesis of the $CuCo_2O_4$ spinel-type framework was confirmed by the X-ray diffraction (XRD) analysis showing consistent crystallographic diffraction peaks (220), (311), (400), (422), (440), and (533) with the standard card (PDF#78-2177) (Figure 2a).[30] After Mn doping, the diffraction peaks all exhibited a systematic shift to the low angle direction, among which the displacement of the (311) crystal plane was the most significant, originating from the lattice expansion triggered by the difference in ionic radii between Mn and Co. A weakening of the diffraction peak intensity and a slight broadening of the half height width were also observed, suggesting that the doping process may lead to a decrease in crystallinity. The Raman analysis of $CuCo_2O_4$ exhibited characteristic peaks at about 475, 521, 627, and 684 cm^{-1} attributed to the E_{2g}, F_{2g}, and A_{1g} vibrational modes of CoO_6 octahedral (Figure 2b).[31] Since the spectral overlap between the F_{2g} vibrational mode of CuO_4 tetrahedron (190 cm^{-1}) and the F_{2g} vibrational mode of tetrahedral CoO_4 tetrahedron (195 cm^{-1}), prompting that the characteristic signals of CuO_4 tetrahedron were not effectively recognized.[32, 33] The Raman peak of A_{1g} in $CuCo_2O_4$ was shifted toward the low wave number direction, which was originated from the lattice substitution effect of CoO_6 octahedral by MnO_6 octahedral with larger radius. The larger ionic radius can induce
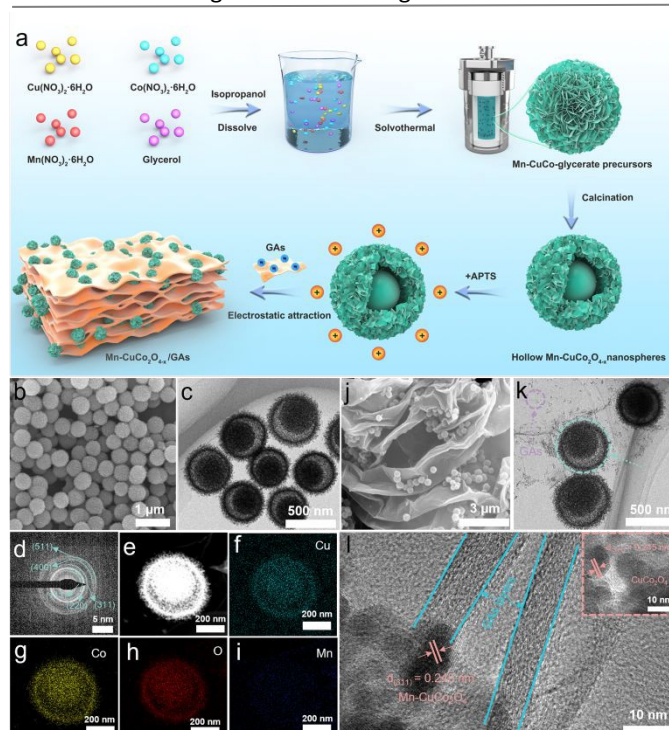
Figure 1 (a) The synthesis schematic of Mn-$CuCo_2O_{4-x}$/GAs. (b) SEM, (c) TEM, (d) SAED, and (e-i) elemental mapping of Mn-$CuCo_2O_{4-x}$. (j) SEM, (k) TEM, and (l) HRTEM images of Mn-$CuCo_2O_{4-x}$/GAs (inset: HRTEM images of Mn-$CuCo_2O_{4-x}$).
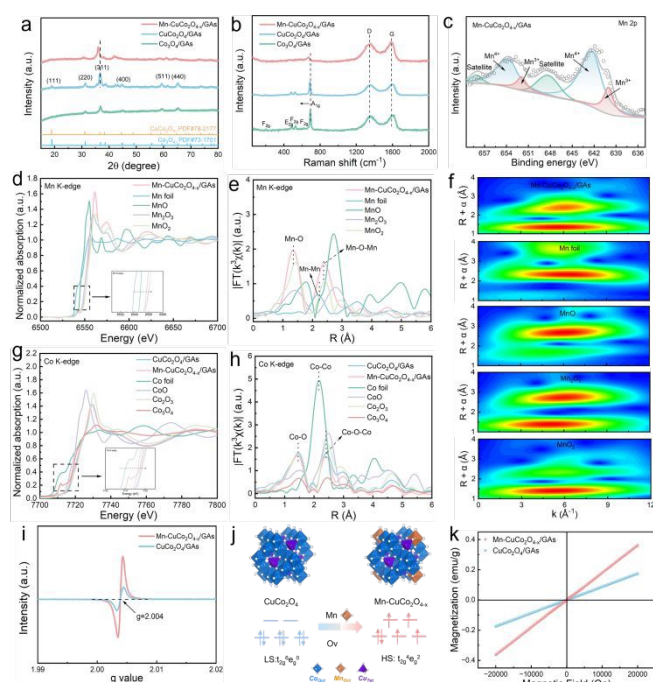
Figure 2 (a) XRD, (b) Raman of Co_3O_4/GAs, $CuCo_2O_4$/GAs, and $Mn-CuCo_2O_{4-x}$/GAs. (c) High-resolution XPS images of Mn 2p of $Mn-CuCo_2O_{4-x}$/GAs. (d) Mn K-edge XANES spectra of $Mn-CuCo_2O_{4-x}$/GAs and the standard reference materials, (e) their corresponding FT-EXAFS spectra. (f) Mn K-edge WT-EXAFS contour plots for $Mn-CuCo_2O_{4-x}$/GAs, Mn foil, MnO, Mn_2O_3 and MnO_2. (g) Co K-edge XANES spectra of $CuCo_2O_4$/GAs and $Mn-CuCo_2O_{4-x}$/GAs and the standard reference materials, (h) their corresponding FT-EXAFS spectra. (i) EPR images of $CuCo_2O_4$/GAs and $Mn-CuCo_2O_{4-x}$/GAs; (j) the influence of Ov on the electron occupancy of Co 3d orbitals. (k) magnetic hysteresis loops of $CuCo_2O_4$/GAs and $Mn-CuCo_2O_{4-x}$/GAs.

local lattice distortion, leading to an increase in metal-oxygen bond length and structural stress, which is consistent with the theoretical model of cation substitution-induced bond length rearrangement.[34] Meanwhile, the characteristic vibrational modes of the D and G bands of the graphitic carbon layer of GAs were detected in Raman spectra, confirming the effective coupling of $CuCo_2O_4$ to GAs.

The chemical valence and coordination environments of the elements were characterized using X-ray photoelectron spectroscopy (XPS) analysis. The XPS full spectra revealed characteristic peaks associated with $Mn-CuCo_2O_{4-x}$ and GAs, indicating the successful construction of $CuCo_2O_4$ and GAs composites (Figure S8). The high-resolution XPS spectra of Cu 2p orbital presented characteristic double peaks at 933.9 eV ($2p_{3/2}$) and 954.0 eV ($2p_{1/2}$), confirming that Cu element exists in the +2-valence state in $CuCo_2O_4$ and $Mn-CuCo_2O_{4-x}$ (Figure S9).[32] Remarkably, the doping of Mn did not change the chemical state of Cu since the binding energy positions and ratios of the two orbitals were not changed. The high-resolution XPS spectra of Mn 2p orbital was divided into divided into Mn $2p_{3/2}$ and Mn $2p_{1/2}$, and the predominant oxidation state of Mn in the samples was Mn^{4+} (Figure 2c).[35] The Co 2p orbital of

$CuCo_2O_4$ exhibited double state features at 779.7/781.5 eV ($2p_{3/2}$) and 796.6/794.7 eV ($2p_{1/2}$), confirming that Co^{2+} and Co^{3+} coexist in the material, and Co^{3+} occupies the main component (Figure S10).[32, 36] Notably, the decrease in the Co^{3+}/Co^{2+} ratio in $Mn-CuCo_2O_{4-x}$ confirmed the preferential occupation of CoO_6 octahedral sites by Mn^{4+}. The O 1s orbitals presented peaks at 529.6, 531.1, and 532.6 eV, corresponding to metal-oxygen (M-O), Ov, and H_2O, respectively, and the Ov concentration of $Mn-CuCo_2O_{4-x}$ was higher than that of $CuCo_2O_4$ (Figure S11).[37] X-ray absorption spectroscopy (XAS) elucidated the electronic state and local coordination of metal elements. Based on the linear combination fitting of the absorption edge positions (Figure 2d and Figure S12a), the oxidation state of Mn in $Mn-CuCo_2O_{4-x}$ was found to be +3.8, which is consistent with the XPS results. Extended X-ray absorption fine structure (EXAFS) analysis of the Mn K-edge (Figure 2e and Figure S13) revealed no evidence of Mn-Mn bond, confirming the atomic dispersion of Mn and absence of clusters. The wavelet transform (WT) spectroscopy in R-space (Figure 2f) of Mn foil, MnO, Mn_2O_3, MnO_2, and $Mn-CuCo_2O_{4-x}$ demonstrated spectral similarity between $Mn-CuCo_2O_{4-x}$ and octahedrally coordinated MnO_2. These results confirm an octahedral coordination environment for Mn, supporting its primary substitution at octahedral Co sites. The normalized Co K-edge X-ray absorption near-edge structure (XANES) spectra (Figure 2g and Figure S12b) of $CuCo_2O_4$ located between Co_3O_4 and Co_2O_3, but closer to Co_2O_3, indicating that Co was predominantly +3 valence in $CuCo_2O_4$. In contrast, the Co K-edge XANES spectra of $Mn-CuCo_2O_{4-x}$ was shifted towards lower energy, suggesting that the substitution of Co^{3+} by Mn^{4+} leads to an increase in the Co^{2+} ratio. Co K-edge EXAFS analysis (Figure 2g) revealed a significant reduction in oscillation amplitude for $Mn-CuCo_2O_{4-x}$ compared to pristine $CuCo_2O_4$, indicative of increased local structural disorder around Co atoms induced by the incorporation of high-valent Mn^{4+} ion. Both the Co K-edge EXAFS spectra of $CuCo_2O_4$ and $Mn-CuCo_2O_{4-x}$ and their corresponding R-space WT spectra (Figures S14- S15) show no evidence of Co–Co bonding contributions. Moreover, the EXAFS fitting result（Table S2）of the first-shell peak for $CuCo_2O_4$ and $Mn-CuCo_2O_{4-x}$ revealed that the Introduction of Ov reduces the average Coordination number of Co.

Prior research has indicated that the addition of metal doping can create lattice distortions and reduce the strength of the metal-oxygen bond, thereby promoting the creation of oxygen vacancies (Ov).[38] Consequently, we analyzed the variations in Ov concentration in the samples using electron paramagnetic resonance (EPR) tests. Compared with $CuCo_2O_4$/GAs, $Mn-CuCo_2O_{4-x}$/GAs exhibited the significantly enhanced signal intensity in EPR spectra, confirming the elevated Ov concentration (Figure 2i). Since Ov are positively charged defect, they would release free electrons into the surroundings to maintain electrical neutrality. These electrons can be trapped by neighboring Co^{3+} to form transient Co^{2+}, enhancing the spin-state of Co^{3+}. In the pristine $CuCo_2O_4$, Co^{3+} is usually in a LS state ($t_{2g}^6 e_g^0$) with a high octahedral coordination field splitting energy, the electrons preferentially populate the t_{2g} orbitals in the lower energy levels (Figure 2j). After the introduction of Ov,

Journal Name

ARTICLE

leading to the localized lattice distortion and ligand field splitting energy below a critical value. At this point, Co^{3+} transitions from LS state to HS state ($t_{2g}^4 e_g^2$), and the number of unpaired electrons increases to four. To validate the proposed the introduction of Ov altering Co^{3+} spin-state, we measured sample magnetism via vibrating sample magnetometry. As displayed in Figure 2k, original $CuCo_2O_4$ exhibited a weak saturation magnetization intensity whereas the saturation magnetization intensity was significantly increased by the introduction of Ov. This phenomenon indicated Ov may induce the transition of Co^{3+} from LS to HS state through modulation of the localized crystal field and electron occupation, leading to a larger number of spin electrons. In summary, Ov can significantly enhance the number of spin-polarized electrons via triggering the HS state transition of Co^{3+}, promoting a more effective "spin promoter" for the orbital interaction between the catalyst and the *NO intermediate.

3.2 Electrocatalytic Performance for the NO_3^--RR

The electrocatalytic activities of Co_3O_4/GAs, $CuCo_2O_4$/Gas, and Mn-$CuCo_2O_{4-x}$/GAs were assessed in an H-type cell. NO_3^-, NO_2^-, and NH_4^+ concentrations during eNO_3^-RR were quantified via UV-Vis spectrophotometry (Figures S16-S18). The linear sweep voltammetry (LSV) curves revealed enhanced current densities for Co_3O_4/GAs, $CuCo_2O_4$/Gas, and Mn-$CuCo_2O_{4-x}$/GAs versus NO_3^--free systems, confirming their intrinsic NO_3^- reduction activity (Figure 3a). Notably, $CuCo_2O_4$/GAs exhibited higher current density than Co_3O_4/GAs, implicating synergistic advantages of Cu-Co bimetallic sites in eNO_3^-RR. Additionally, Mn-$CuCo_2O_{4-x}$/GAs possessed larger current density and more positive starting reduction potential compared with $CuCo_2O_4$/GAs, suggesting Mn doping further can enhance the catalytic activity of eNO_3^-RR. Electrochemical impedance spectra (EIS)-based analysis of electron transport kinetics displayed Mn-$CuCo_2O_{4-x}$/GAs possessed the smallest capacitive arc radius in the Nyquist plot (Figure 3b). Moreover, The R_{ct} values showed a dramatic and conclusive trend: Co_3O_4/GAs (66.17 Ω) > $CuCo_2O_4$/GAs (26.69 Ω) > Mn-$CuCo_2O_{4-x}$/GAs (15.64 Ω), which was in excellent agreement with the observed catalytic activity (Table S3). This decrease in R_{ct} unequivocally demonstrated that the charge transfer kinetics for eNO_3^-RR was significantly enhanced upon introducing Cu, indicating that the bimetallic synergy drastically facilitated the electron transfer process. Most impressively, the Mn-$CuCo_2O_{4-x}$/GAs achieved the lowest R_{ct} value, which provided direct electrochemical evidence that the Mn doping and the induced Ov created a more favorable electronic structure, further accelerating the rate-determining electron transfer steps in the eNO_3^-RR. Electrochemical active surface area (ECSA) was quantified by electrochemical double-layer capacitance (C_{dl}) measurements from cyclic voltammetry (CV) in non-Faradaic windows (Figure S19). Higher C_{dl} value for Mn-$CuCo_2O_{4-x}$/GAs (5.20 mF cm^{-2}) versus Co_3O_4/GAs (1.62 mF cm^{-2}) and $CuCo_2O_4$/GAs (2.22 mF cm^{-2}), confirming that Cu-Co bimetallic synergism together with Mn doping can increase the active site density, thus enhancing the intrinsic activity of eNO_3^-RR. Based on the LSV results, -0.4 to -0.8 V vs. RHE was identified as the characteristic potential window. The chronoamperometry quantified the FE and NH_3-N

yield rates of catalysts (Figure S20). The trend of volcanic distribution of FE for each catalyst confirmed the existence of a critical starting overpotential for eNO_3^-RR (Figure 3c). Excessively negative potentials attenuated FE due to competing hydrogen evolution reaction (HER). Mn-$CuCo_2O_{4-x}$/GAs exhibited higher FE than both counterparts across tested potentials, achieving a maximum of 98.37% at -0.6 V vs. RHE. The Mn-$CuCo_2O_{4-x}$/GAs presented the highest NH_3-N yield rate at all potentials, especially at the voltage corresponding to the optimal FE, the NH_3-N yield rate of 2.14 mg/h/cm^2 (Figure 3d). Additionally, the selectivity of the catalysts was further evaluated based on the yield rate and FE of the intermediate NO_2^- (Figure S21). As the applied voltage increased, both the NO_2^- yield rate and corresponding FE of the three catalysts exhibited a gradual decrease. Among them, the Mn-$CuCo_2O_{4-x}$/GAs maintained the lowest values for both metrics, indicating its greater ability to promote the further conversion of the intermediate NO_2^-. This highlights the outstanding selectivity of this catalyst in the NO_3^- reduction process.

The properties of the nitrogen source in NH_3-N were verified through blank control. The results revealed almost negligible ammonia production in the blank control, clearly confirming the nitrogen in the product originated from NO_3^- rather than from environmental pollutants (Figure S22). ^{1}H-nuclear magnetic resonance (^{1}H-NMR) was used to monitor the dynamics of the nitrogen conversion pathways. When $^{15}NO_3^-$ and $^{14}NO_3^-$ were employed as nitrogen sources, the corresponding $^{15}NH_4^+$ and $^{14}NH_4^+$ showed characteristic double- peak and triple-peak splitting patterns, providing direct evidence for the directional conversion of NO_3^- to NH_3 (Figure 3e). Although Mn-$CuCo_2O_{4-x}$/GAs had excellent catalytic activity, the performance comparison between this material and similar advanced catalysts still needs to be clarified. To this end, we systematically summarized the recent literature for the low-
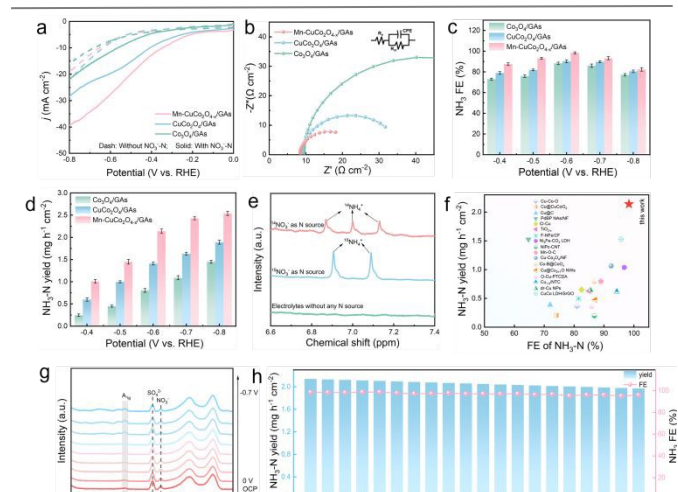
Figure 3 (a) LSV curves, (b) EIS curves, (c) FE, and (d) NH_3-N yield rates of Co_3O_4/GAs, $CuCo_2O_4$/GAs, and Mn-$CuCo_2O_{4-x}$/GAs. (e) ^{1}H NMR spectra for $^{14}NO_3^-$ and $^{15}NO_3^-$ electrolyte after 1 h electrolysis. (f) Comparison of eNO_3^-RR performance of Mn-$CuCo_2O_{4-x}$/GAs with reported electrocatalysts. (g) In-situ Raman spectra of Mn-$CuCo_2O_{4-x}$/GAs at different voltages. (h) The cyclic stability tests of Mn-$CuCo_2O_{4-x}$/GAs.

concentration NO_3^- system (Figure 3e and Table S4). Both the FE and NH_3-N yield rate of Mn-$CuCo_2O_{4-x}$/GAs was significantly better than other reported systems, fully demonstrating the leading position of this catalyst in eNO_3^-RR. The structural evolution of the Mn-$CuCo_2O_{4-x}$/GAs electrocatalyst during the eNO_3^-RR was dynamically tracked using in-situ Raman spectroscopy. In the absence of GAs, the characteristic Raman peak corresponding to the A_{1g} vibrational mode of Mn-$CuCo_2O_{4-x}$ exhibited a rapid decrease in intensity as the applied potential shifted negatively, indicating insufficient structural stability under operating conditions (Figure S23). In contrast, after the introduction of GAs, the same characteristic Raman mode remained clearly detectable even at highly negative potentials up to -0.7 V vs. RHE, demonstrating significantly enhanced structural integrity (Figure 3g). This pronounced contrast underscores the critical role of GAs in stabilizing the active material through strong interfacial interactions, which effectively anchor the Mn-$CuCo_2O_{4-x}$, prevent agglomeration or dissolution, and thus maintain the structural and catalytic durability of the Mn-$CuCo_2O_{4-x}$/GAs composite throughout the reaction. The FE and NH_3-N yield rate of the system exhibited only minor fluctuations during the continuous electrolysis test for up to 20 h, demonstrating excellent cycling stability (Figure 3h). The catalysts before and after the reaction were systematically characterized by XRD and TEM, and neither the crystal structure nor the microscopic morphology significantly changed, further verifying the excellent structural stability of Mn-$CuCo_2O_{4-x}$/GAs at the microscopic level (Figures S24-S25).

3.3 Reaction Pathways and Mechanisms

Time-resolved electrochemical mass spectrometry (DEMS) identified key eNO_3^-RR intermediates on $CuCo_2O_4$/GAs and Mn-$CuCo_2O_{4-x}$/GAs (Figures 4a-b and Figure S26). m/z signals at 15, 16, 17, 30, and 31 revealed *NH, *NH_2, *NO, HNO, and NH_3 intermediate generation. Notably, the characteristic signal peak intensity of the relevant intermediates on Mn-$CuCo_2O_{4-x}$/GAs was significantly higher than $CuCo_2O_4$/GAs, suggesting the introduction of Ov can significantly enhance the generation capacity of the key intermediates. Operando Fourier transformed infrared spectroscopy (FT-IR) tracked real-time evolution of surface intermediates during reaction (Figure 4c and Figure S27). The vibrational peaks at 1650 cm^{-1} (δH-O-H) and 3300 cm^{-1} (vH-O-H) corresponded to interfacial water adsorption and cleavage.[39, 40] The progressive intensification of vibrational signatures at 1460 cm^{-1} and 3200 cm^{-1} can be unambiguously assigned to the stretching vibrations of N-H bonds in NH_3 molecules.[41, 42] Based on the key intermediate species and their dynamic evolution patterns monitored online in this study, combined with the mechanistic models reported in the literature, we systematically deduced and constructed the reaction pathway dominated by the stepwise hydrogenation of *NO (Figure S28). The dynamic evolutionary behavior of active hydrogen species (*H) during eNO_3^-RR process was systematically investigated by in-situ EPR technique (Figures 4d). The 5,5-dimethyl-1-pyrroline-N-oxide (DMPO)-*H spin adduct signal intensity for Mn-$CuCo_2O_{4-x}$/GAs doubled that of $CuCo_2O_4$/GAs in 0.1 M Na_2SO_4 electrolyte lacking NO_3^-, confirming Mn doping effectively promoted the

hydrolytic dissociation to generate *H. Intriguingly, upon introducing 10 mM NO_3^- into the electrolyte, the characteristic signal intensity corresponding to the *H on Mn-$CuCo_2O_{4-x}$/GAs exhibited significant attenuation during the electrocatalytic process. This apparent inhibitory effect may stem from the rapid depletion caused by *H and NO_3^- reactions. These findings demonstrate that NO_3^- reduction on Mn-$CuCo_2O_{4-x}$/GAs proceeded via an *H-mediated indirect pathway, and the Ov promoted the hydrogenation process of nitrogen-containing intermediates. To further evaluate the interfacial H_2O dissociation capability of the prepared catalysts, kinetic isotope effect (KIE) tests were conducted by replacing H_2O with D_2O. The KIE value was calculated by comparing the current densities measured in H_2O and D_2O, thereby revealing the dynamic process of *H transfer during H_2O dissociation (Figure S29). Results indicated that Mn-$CuCo_2O_{4-x}$/GAs exhibits an average KIE value of 1.24, significantly lower than other reference electrocatalysts, demonstrating that the introduction of Ov effectively promotes interfacial H_2O dissociation. Concurrently, it also demonstrated that Ov possesses a significant interface water regulation behavior. Gibbs free energy change (ΔG) plots for $CuCo_2O_4$ and Mn-$CuCo_2O_{4-x}$ in eNO_3^-RR are shown in Figure 4e. Both $CuCo_2O_4$ and Mn- $CuCo_2O_4$ synthesize NH_3 via the 8-electron reduction pathway (NO_3^-→*NO_3→*HNO_3→*NO_2→*NO→*HNO→*NH→*NH_2→*NH_3→ NH_3) (Figures S30-S31). The ΔG profile identified *NO hydrogenation to *HNO as the rate-determining step (RDS), exhibiting the highest energy barrier. Apparently, Ov lowered the RDS energy barrier from 1.39 eV to 0.41 eV, thereby enhancing eNO_3^-RR reaction kinetics. Promoting the dissociation of H_2O to produce *H and inhibiting the coupling of *H to produce H_2 are essential to enhance the performance of eNO_3^-RR. As illustrated in Figure 4f and Figures S32-S33, the H_2O adsorption energy of Mn-$CuCo_2O_{4-x}$ (-0.41 eV) was significantly negatively shifted compared with that of $CuCo_2O_4$ (-0.19 eV), indicating that its activation of H_2O was largely enhanced. The H_2O dissociation energy barrier was reduced from 0.32 eV to 0.14 eV, effectively promoting the generation of *H active species. Meanwhile, the ΔG of H_2 generation on the surface of Mn-$CuCo_2O_{4-x}$ (ΔG = 0.38 eV) showed a significant positive shift compared with that of $CuCo_2O_4$ (ΔG = 0.07 eV), suggesting Ov significantly inhibited the generation of H_2 by the coupling of *H. In conclusion, Ov can lower the hydrogenation barrier of *NO → *HNO, accelerating the H_2O dissociation and inhibiting the HER side reaction, thereby enhancing selective NO_3^--to- NH_3 conversion.

After identifying *NO→*HNO as RDS, density functional theory (DFT) deciphered orbital interaction mechanisms between $CuCo_2O_4$/Mn-$CuCo_2O_{4-x}$ and reaction intermediates. Density of states analysis of *NO and *HNO intermediates revealed pronounced spin asymmetry in *NO across spin-up/down channels, contrasting with spin symmetry in *HNO (Figure 4g). This shift in spin configuration revealed a spin rearrangement phenomenon occurring during the reaction, which essentially stems from the pairing process of unpaired electrons. Differential charge density analysis revealed *NO adsorbed on the surface of Mn-$CuCo_2O_{4-x}$ (0.28 |e|) had a higher electron

ARTICLE
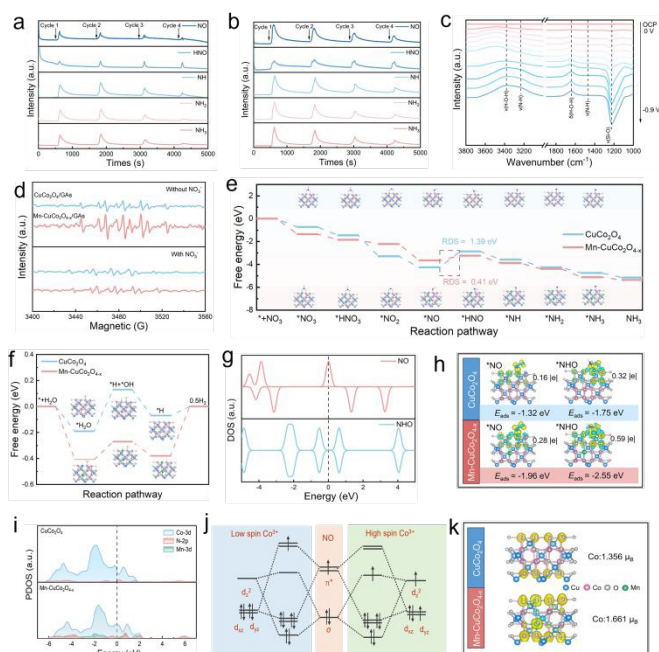
Figure 4 (a, b) Online DEMS spectra of $CuCo_2O_{4-x}$/GAs and Mn-$CuCo_2O_{4-x}$/GAs. (c) In-situ FT-IR spectra of Mn-$CuCo_2O_{4-x}$/GAs. (d) EPR spectra of $CuCo_2O_{4-x}$/GAs and Mn-$CuCo_2O_{4-x}$/GAs in electrolytes without/ with NO_3^-. Gibbs free energy profiles for (e) eNO_3^-RR and (f) HER on $CuCo_2O_4$ and Mn-$CuCo_2O_{4-x}$. (g) DOS of *NO and *HNO species. (h) Differential charge density of critical intermediates adsorbed on $CuCo_2O_4$ and Mn-$CuCo_2O_{4-x}$ interfaces. (i) PDOS analyses of *NO intermediates adsorbed on $CuCo_2O_4$ and Mn-$CuCo_2O_{4-x}$. (j) Schematic illustration of orbital hybridization of Co and *NO in different spin states. (k) Spin charge density of $CuCo_2O_4$ and Mn-$CuCo_2O_{4-x}$.

transfer number compared with $CuCo_2O_4$ (0.16 |e|), suggesting that Ov intensified the interfacial electron transfer process and the bonding tendency to the *NO intermediates was stronger (Figure 4h).[43] Meanwhile, enhanced *NO adsorption was observed on Mn-$CuCo_2O_{4-x}$ (-1.96 eV) relative to $CuCo_2O_4$ (-1.32 eV). Thus, spin-state transition promoted *NO adsorption on catalysts, corroborated by projected density of states (PDOS) analysis. Figure 4i revealed a significant overlap region between the hybridization of the Co-3d orbitals in Mn-$CuCo_2O_{4-x}$ and the N-2p orbitals of *NO and the hybridization energy intervals skewed towards the Fermi energy level, suggesting the existence of a stronger orbital interaction in Mn-$CuCo_2O_{4-x}$ and *NO.[43] Furthermore, Mn-$CuCo_2O_{4-x}$ enhanced *NO hydrogenation by stabilizing critical *HNO intermediates, which can be illustrated by the fact that *HNO adsorbed on Mn-$CuCo_2O_{4-x}$ exhibited a larger electron transfer number and a more negative adsorption energy than $CuCo_2O_{4-x}$.[44] Based on the previous analysis of the orbital configuration of the Co high spin-state ($t_{2g}^4e_g^2$), its $d_{xz}/d_{yz}/d_{z^2}$ orbitals can form a directional hybridization with the σ/π^* antibonding orbitals of *NO, whereas the d_{xy} and $d_{x^2-y^2}$ orbitals are excluded from the effective coupling regime due to symmetry mismatch.[43, 45] In this hybridization, the d_{z^2} orbitals of Co can accept electron

occupation from the σ orbitals while the d_{xz}/d_{yz} orbitals fed electrons back to the π^* orbitals. This Co 3d ($d_{xz}/d_{yz}/d_{z^2}$)-*NO 2p asymmetrical orbital hybridization enhanced the adsorption of *NO intermediates, weakened the N-O bond, thereby facilitating *NO hydrogenation to *HNO (Figure 4j). The unique catalytic properties of $CuCo_2O_4$ and Mn-$CuCo_2O_{4-x}$ can also be illustrated by the magnetic moment of Co orbitals. The magnetic moment of Co increased from 1.356 μ_B to 1.661 μ_B after the introduction of Ov (Figure 4k). The elevated magnetic moment is directly associated with the elevated occupancy of the HS state of Co, and the increase in the number of its unpaired electrons facilitates the electron exchange between the active site and *NO, accelerating the kinetics of *NO hydrogenation. To summarize, by combining experimental characterization with DFT calculations, we revealed that the elevation of the internal Co spin state in the Cu-Co bimetallic active sites can further enhance the Cu-Co synergistic catalysis through the role of orbital hybridization.

4. Conclusions

In summary, the spin-state of Co^{3+} in spinel $CuCo_2O_4$ was modulated by Mn doping-driven Ov strategy, and the controllable transition from LS state to HS state was successfully realized, significantly enhancing the Cu-Co bimetallic synergistic catalysis. Experiments and DFT revealed the HS state Co^{3+} can optimize the adsorption of the key intermediate *NO and hydrogenation step via enhancing the asymmetric hybridization of the Co 3d ($d_{xz}/d_{yz}/d_{z^2}$)-*NO 2p orbitals, thus accelerating the eNO_3^-RR kinetic process. The Mn-$CuCo_2O_{4-x}$/GAs demonstrated superior electrocatalytic performance, achieving an NH_3 yield rate of 2.14 mg/h/cm^2 and a Faradaic efficiency of 98.37% at -0.6 V vs. RHE, outperforming both Co_3O_4/GAs, $CuCo_2O_4$/GAs, as well as previously reported catalysts. This work proposes the first theoretical correlation between spin-state modulation and bimetallic synergistic catalysis, offering a new avenue for the design of high-performance catalytic systems for the deep purification of water pollutants and resource recovery.

Author contributions

Ke Wang and Tong Zhao: data curation and writing – original draft. Hou Wang and Shiyu Zhang: investigation. Rupeng Wang: formal analysis. Meng Wang: writing – review & editing. Zixiang He: supervision. Shih-Hsin Ho: funding acquisition.

Conflicts of interest

There are no conflicts to declare.

Data availability

The authors confirm that the data supporting the findings of this study are available within the article and its ESI.

Acknowledgements

Chemical Science Accepted Manuscript

References

1   J. G. Chen, R. M. Crooks, L. C. Seefeldt, K. L. Bren, R. M. Bullock, M. Y. Darensbourg, P. L. Holland, B. Hoffman, M. J. Janik, A. K. Jones, M. G. Kanatzidis, P. King, K. M. Lancaster, S. V. Lymar, P. Pfromm, W. F. Schneider and R. R. Schrock, *Science*, 2018, **360**, eaar6611.

2   Y. Wang, C. Wang, M. Li, Y. Yu and B. Zhang, *Chem. Soc. Rev.*, 2021, **50**, 6720-6733.

3   P. H. van Langevelde, I. Katsounaros and M. T. M. Koper, *Joule*, 2021, **5**, 290-294.

4   Y. Xue, Q. Yu, Q. Ma, Y. Chen, C. Zhang, W. Teng, J. Fan and W.-x. Zhang, *Environ. Sci. Technol.*, 2022, **56**, 14797-14807.

5   W. Duan, Y. Chen, H. Ma, J.-F. Lee, Y.-J. Lin and C. Feng, *Environ. Sci. Technol.*, 2023, **57**, 3893-3904.

6   S. Han, H. Li, T. Li, F. Chen, R. Yang, Y. Yu and B. Zhang, *Nat. Catal.*, 2023, **6**, 402-414.

7   F.-Y. Chen, Z.-Y. Wu, S. Gupta, D. J. Rivera, S. V. Lambeets, S. Pecaut, J. Y. T. Kim, P. Zhu, Y. Z. Finfrock, D. M. Meira, G. King, G. Gao, W. Xu, D. A. Cullen, H. Zhou, Y. Han, D. E. Perea, C. L. Muhich and H. Wang, *Nat. Nanotechnol.*, 2022, **17**, 759-767.

8   K. Fan, W. Xie, J. Li, Y. Sun, P. Xu, Y. Tang, Z. Li and M. Shao, *Nat. Commun.*, 2022, **13**, 7958.

9   K. Wang, R. Mao, R. Liu, J. Zhang, H. Zhao, W. Ran and X. Zhao, *Nat. Water*, 2023, **1**, 1068-1078.

10   S. Zhang, J. Wu, M. Zheng, X. Jin, Z. Shen, Z. Li, Y. Wang, Q. Wang, X. Wang, H. Wei, J. Zhang, P. Wang, S. Zhang, L. Yu, L. Dong, Q. Zhu, H. Zhang and J. Lu, *Nat. Commun.*, 2023, **14**, 3634.

11   G.-F. Chen, Y. Yuan, H. Jiang, S.-Y. Ren, L.-X. Ding, L. Ma, T. Wu, J. Lu and H. Wang, *Nat. Energy*, 2020, **5**, 605-613.

12   H. Liu, X. Lang, C. Zhu, J. Timoshenko, M. Rüscher, L. Bai, N. Guijarro, H. Yin, Y. Peng, J. Li, Z. Liu, W. Wang, B. R. Cuenya and J. Luo, *Angew. Chem. Int. Edit.*, 2022, **61**, e202202556.

13   W. He, J. Zhang, S. Dieckhöfer, S. Varhade, A. C. Brix, A. Lielpetere, S. Seisel, J. R. C. Junqueira and W. Schuhmann, *Nat. Commun.*, 2022, **13**, 1129.

14   J.-Y. Fang, Q.-Z. Zheng, Y.-Y. Lou, K.-M. Zhao, S.-N. Hu, G. Li, O. Akdim, X.-Y. Huang and S.-G. Sun, *Nat. Commun.*, 2022, **13**, 7899.

15   Z. Ren, K. Shi, Z. Meng, M. D. Willis and X. Feng, *ACS Energy Lett.*, 2024, **9**, 3849-3858.

16   R. Yan, H. Yin, X. Zuo, W. Peng, X. Zhu, L. Shi, J. Hou, D. Wang, F. Ye, J. Li, B. Mao and C. Hu, *Appl. Catal. B-Environ. Energy y*, 2025, **361**, 124609.

17   Z. Gu, Y. Zhang, X. Wei, Z. Duan, Q. Gong and K. Luo, *Adv. Mater.*, 2023, **35**, 2303107.

18   Y. Zhou, R. Duan, H. Li, M. Zhao, C. Ding and C. Li, *ACS Catal.*, 2023, **13**, 10846-10854.

19   C. Zhou, C.-Z. Yuan, F. Jing, C.-H. Li, H. Zhao, Y. Sun and W. Yuan, *J. Energy Chem.*, 2025, **106**, 142-150.

20   Y. Xie, Y. Feng, S. Zhu, Y. Yu, H. Bao, Q. Liu, F. Luo and Z. Yang, *Adv. Mater.* 2025, **37**, 2414801.

21   M. Duan, C. Huang, G. Zhang, H. Shi, P. Zhang, L. Li, T. Xu, Z. Zhao, Z. Fu, J. Han, Y. Xu and X. Ding, *Angew. Chem. Int. Edit.*, 2024, **63**, e202318924.

22   L. Zhao, C. Xin, C. Yu, Y. Xing, Z. Wei, H. Zhang, T. Fei, S. Liu, H. Zhang and T. Zhang, *InfoMat*, 2025, **7**, e12634.

23   M. Xu, H. Zhou, X. Lv, Y. Fang, X. Tu, F. Wang, Q. Han, X. Wang and G. Zheng, *Adv. Mater.,* 2025, **n/a**, 2505286.

24   J. Qi, Q. Bai, X. Bai, H. Gu, S. Lu, S. Chen, Q. Li, X. Yang, J. Wang and L. Wang, *Adv. Sci.*, 2025, **n/a**, 2503665.

25   S. Zhang, W. Zhao, J. Liu, Z. Tao, Y. Zhang, S. Zhao, Z. Zhang and M. Du, *Adv. Sci.,* 2024, **11**, 2407301.

26   J. Ding, Z. Wei, F. Li, J. Zhang, Q. Zhang, J. Zhou, W. Wang, Y. Liu, Z. Zhang, X. Su, R. Yang, W. Liu, C. Su, H. B. Yang, Y. Huang, Y. Zhai and B. Liu, *Nat. Commun.*, 2023, **14**, 6550.

27   J. Qiao, C. Lu, L. Kong, J. Zhang, Q. Lin, H. Huang, C. Li, W. He, M. Zhou and Z. Sun, *Adv. Funct. Mater.*, 2024, **34**, 2409794.

28   H. Xue, J. Wang, H. Cheng, H. Zhang, X. Li, J. Sun, X. Wang, L. Lin, Y. Zhang, X. Liao and Y. He, *Appl. Catal. B-Environ. Energy*, 2024, **353**, 124087.

29   Z. Huang, Y. Liang, Z. Wu, Y. Kong, M. Bai, M. Li, B. Hong, T. Huang, S. Huang, H. Chen and S. Zhang, *Adv. Mater.*, 2025, **37**, 2410318.

30   Y.-X. Zhang, Y.-D. Li, A.-K. Du, Y. Wu and J.-B. Zeng, *J. Mater. Sci. Technol.*, 2024, **173**, 114-120.

31   J. Geltmeyer, G. Vancoillie, I. Steyaert, B. Breyne, G. Cousins, K. Lava, R. Hoogenboom, K. De Buysser and K. De Clerck, *Adv. Funct. Mater.*, 2016, **26**, 5987-5996.

32   K. Liu, X. Gao, C.-X. Liu, R. Shi, E. C. M. Tse, F. Liu and Y. Chen, *Adv. Energy Mater.*, 2024, **14**, 2304065.

33   Y. Chen, Q. Li, R. Su, Y. Gao, N. An, Y. Rong, X. Xu, D. Ma, Y. Wang and B. Gao, *Water Res.*, 2025, 123765.

34   H. Lin, J. Wei, Y. Guo, Y. Li, X. Lu, C. Zhou, S. Liu and Y.-y. Li, *Adv. Funct. Mater.*, 2024, **34**, 2409696.

35   X. Guo, W. Cai, Y. Zhuo and S. Liu, *Appl. Catal. B-Environ. Energy*, 2025, **373**, 125354.

36   L. Wu, Q. Wu, Y. Han, D. Zhang, R. Zhang, N. Song, X. Wu, J. Zeng, P. Yuan, J. Chen, A. Du, K. Huang and X. Yao, *Adv. Mater.*, 2024, **36**, 2401857.

37   K. Wang, T. Zhao, N.-Q. Ren and S.-H. Ho, *Water Res.*, 2024, **265**, 122304.

38   Q. Deng, H. Li, K. Pei, L. W. Wong, X. Zheng, C. S. Tsang, H. Chen, W. Shen, T. H. Ly, J. Zhao and Q. Fu, *ACS Nano*, 2024, **18**, 33718-33728.

39   M. Xie, G. Zhu, H. Yang, B. Liu, M. Li, C. Qi, L. Wang, W. Jiang, P. Qiu and W. Luo, *Adv. Energy Mater.*, 2024, **14**, 2401717.

40   J. Li, H. Li, K. Fan, J. Y. Lee, W. Xie and M. Shao, *Chem Catal.*, 2023, **3**, 100638.

41   Y. Huang, C. He, C. Cheng, S. Han, M. He, Y. Wang, N. Meng, B. Zhang, Q. Lu and Y. Yu, *Nat. Commun.*, 2023, **14**, 7368.

42   J. Ni, J. Yan, F. Li, H. Qi, Q. Xu, C. Su, L. Sun, H. Sun, J. Ding and B. Liu, *Adv. Energy Mater.*, 2024, **14**, 2400065.

43   J. Liang, S. Deng, Z. Li, M. Zhou, S. Wang, Y. Su, S. Yang and H. Li, *Adv. Mater.*, 2025, **37**, 2418828.

44   J. Dai, Y. Tong, L. Zhao, Z. Hu, C.-T. Chen, C.-Y. Kuo, G. Zhan, J. Wang, X. Zou, Q. Zheng, W. Hou, R. Wang, K. Wang, R. Zhao, X.-K. Gu, Y. Yao and L. Zhang, *Nat. Commun.*, 2024, **15**, 88.

45   Y. Sun, S. Sun, H. Yang, S. Xi, J. Gracia and Z. J. Xu, *Adv. Mater.* 2020, **32**, 2003297.

View Article Online
DOI: 10.1039/D5SC06823A

The authors confirm that the data supporting the findings of this study are available within the article and its ESI.

Chemical Science Accepted Manuscript